The Climate Hazards Center Coupled Model Intercomparison Project Phase 6 (CHC-CMIP6) climate projection dataset

Data Descriptor

Synopsis: This document provides an overview of the Climate Hazards Center Coupled Model Intercomparison Project Phase 6 climate projection dataset (CHC-CMIP6).

This dataset has been developed to support the analysis of climate-related hazards over the 1980s-to-the-near present and in the near-future, as represented by 2030 and 2050 high resolution daily projections of minimum and maximum temperatures, precipitation, relative humidity, vapor pressure deficits (VPD), and maximum wet bulb globe temperatures ($WBGT_{max}$). The high-resolution Climate Hazards center InfraRed Precipitation with Stations (CHIRPS) and Climate Hazards center InfraRed Temperature with Stations (CHIRTS) products, augmented by ERA5 relative humidity fields, form the basis of the observational record. Large CMIP6 ensembles from the 2-4.5 and 5-8.5 Shared Socioeconomic Pathway (SSP) scenarios were used to create 'delta' fields which were used to perturb the observations, thereby generating high-resolution (0.05°) 2030 and 2050 projections of precipitation, temperature, relative humidity, VPD, and WBGT. These delta fields are based on the CMIP6 changes between the observed period, 1983-2016, and the projected periods, 2025-2035 and 2045-2055.

Contents:

For any questions about this data product or document, please contact:

- For questions about the ftp site or data management: geogpete (at) gmail.com
- For questions about the data or underlying equations: chris.funk (at) geog.ucsb.edu or ewilliams (at) ucsb.edu

Last updated: 4/19/23

1. Overview and Rationale

1.A. Why High-Resolution, Global Observational and Projection Data is Needed

The Climate Hazards Center Coupled Model Intercomparison Project Phase 6 climate projection dataset (CHC-CMIP6) was created to provide high-resolution observation and scenario-based projection hydro-climatic data that can be used to support the identification, monitoring, and analysis of current and future potential hazards in data sparse regions.

Many climate models, such as those used by CMIP, have relatively coarse spatial resolution (typically ~100km). Such models may not be able to distinguish precipitation, temperature, or other climatic gradients across a landscape relevant to many human-environment systems and thus are unable to capture more fine-scale variability in local climatic conditions. Yet many climate hazards are inherently local. Relatively nearby places may have different baseline climatologies, so an absolute change in a climatic variable (e.g. 2° Celsius of warming) may lead to or exacerbate hazards in one place but not the other.

For example, in water-limited growing regions, crop yields will be sensitive to the amount of available soil moisture, which is tightly linked to the amount of growing season precipitation, which can vary across the landscape. Moreover, during germination, many crops are sensitive to very warm air temperatures. Two degrees of warming in a hot, dry place may have a much greater agro-pastoral impact than two degrees of warming in a cool, moist location. Conversely, in terms of human health and labor productivity, two degrees of warming in a hot, humid place may dramatically increase hazards, yet not increase hazards in a cooler or drier place. Further, the changing magnitude of heat waves that impact human health and well-being can vary drastically over short distances (Tuholske *et al*. 2021). These dependencies can create strong, fine-grained links between geography, climate, and hazards. Such dependencies, combined with the very limited number of in situ weather observations in many countries (Funk *et al.* 2019), make it difficult to monitor hydro-climatic extremes. Therefore, high spatial resolution data that accurately captures extremes is crucial for monitoring such potential hazards.

In response to the challenges presented by limited available data on climatic hazards in data-sparse regions, this CHC-CMIP6 observational and projection dataset offers high-resolution (0.05°) hydro-climatic data – minimum temperature (T_{min}), maximum temperature (T_{max}), precipitation, vapor pressure deficits (VPD), and maximum wet bulb globe temperatures ($WBGT_{max}$) – for the current/observed period (1983-2016) and near-future scenarios (2030 and 2050). It also presents counts of T_{max}, T_{min}, VPD, and $WBGT_{max}$ 'extremes' for the observations dataset and each of the scenarios. The CHC-CMIP6 projection dataset retains the high spatial resolution and precision of the CHC temperature and precipitation products while projecting changes in hydro-climatic variables using climate model output.

1.B. The Hydroclimatic Variables: WBGT & VPD

Two of the hydro-climatic variables included in this dataset—maximum $WBGT_{max}$ and VPD—are described in detail here. These variables are particularly relevant for human health and agro-pastoral drought, and moreover are a function of the same physical process. As defined by the Clausius-Clapeyron relationship, warmer air can hold more water vapor (Ahrens 1994:81; Held and Soden 2006). This is measured by saturation vapor pressure (SVP), or the water vapor content required to fully saturate the air at a specific temperature, whereby SVP increases exponentially with temperature. In places and seasons with ample available moisture, with increasing temperatures (and SVP), evaporation will increase, leading to an increase in actual vapor pressure (AVP), maintaining or increasing relative humidity (RH) (Ahrens 1994:82). This combination of high temperatures and humidity can lead to increased heat stress for people in hot, humid regions (measured by WBGT). However, in water-limited environments, evaporation cannot keep pace, so a deficit will grow between the water holding *capacity* of the air (SVP) and how much water vapor is actually held (AVP), leading to greater evaporative demand (measured by VPD), leading to or exacerbating drought in hot, dry regions.

WBGT is a widely-used heat stress metric (Kong and Huber 2022; Budd 2008), which provides an estimate of 'effective temperature' explicitly designed for applications to human health in hot and humid areas (ISO 2017). WBGT measures what temperatures 'feel like' for a person exercising or doing work. As a function of wind speed, radiated heat, temperature, and humidity, it relates to how rapidly humans can cool their bodies through evaporation via sweat (ISO 2017). The advantage of using $WBGT_{max}$, as opposed to meteorological indicators like T_{max}, is that the former accounts for important non-linear biophysical responses (Mora et al. 2017). Humans maintain skin temperatures and core temperatures at 35°C and 37°C. Elevated core temperatures (hyperthermia) occur when core temperatures exceed 42°C (Bynum et al. 1978), though some acclimatization can occur (Bynum et al. 1978, Cheung and McLellan 1998). This acclimatization, however, is limited to improved sweating responses, which are fundamentally limited by high relative values. For $WBGT_{max}$, daily maximum of 30°C has been associated with doubling in mortality rates compared to $WBGT_{max}$ of 20°C among vulnerable populations working outside (Pradham et al. 2019).

Conversely, in water-limited areas, increasing VPD can exacerbate drought conditions by evaporating surface water bodies and decreasing soil moisture (Williams et al. 2020). VPD can also reduce plant productivity, including for pasture and crops (Grossiord et al. 2020; Novick et al. 2016; Lobell et al. 2014; Kath et al. 2022). Plants can 'sense' environmental conditions and adjust their growth rate accordingly (Grossiord et al. 2020; Novick et al. 2016). VPD thus constrains plant productivity via two primary pathways: through the indirect effect of reducing soil moisture via increased evaporation, and the direct effect at the leaf-level of affecting stomatal conductance, or the rate of exchange of water vapor and carbon dioxide (Chapin et al. 2012; Novick et al. 2016). Increased VPD will lead to increased evaporation, thereby reducing surface soil moisture. When soil moisture falls below critical thresholds, the plant will close stomata (Fu et al. 2022; He et al. 2022). Moreover, if the plant senses increased VPD at the leaf-level, it will

partially close stomata to conserve water. While these mechanisms allow plants to survive during dry times, it is at the expense of photosynthesis (Sperry et al. 2017).

Therefore, both daily $WBGT_{max}$ and daily VPD are included in the CHC-CMIP6 dataset to facilitate the identification of those places and seasons with high exposure to heat stress and drought conditions.

1.C. Overview of the CHC-CMIP6 Dataset and Data Access

Table 1 provides an overview of the CHC-CMIP6 data products available for download. The five 'core' daily datasets form the backbone of the CHC-CMIP6 archive, available for the observational period (1983-2016) and for the four projections: 2030_SSP245, 2030_SSP585, 2050_SSP245, and 2050_SSP585. These datasets contain daily 0.05° resolution CHIRPS 2.0 precipitation (based on Funk et al. 2015b), CHIRTS T_{min} and T_{max} (based on Funk et al. 2019), RH_x, RH_{ave}, $WBGT_{max}$, VPD, and SVP. The five 'extremes' datasets include the same scenarios and variables but depict the spatio-temporal observations or projections of extremes for each variable. Finally, the daily 'deltas', used to derive the four projections, depict the changes between the observational and scenario-projection periods for precipitation, temperature, and RH variables.

The data are available as geotifs at: https://data.chc.ucsb.edu/experimental/CHC_CMIP6/

- The /observations/ subdirectory contains 0.05° daily 1983-2016 CHIRTS T_{min} and T_{max}, CHIRPS precipitation, VPD, and $WBGT_{max}$.
- The /YYYY_SSPXXX/ subdirectories contain 0.05° daily CHIRTS T_{min} and T_{max}, CHIRPS precipitation, VPD, and $WBGT_{max}$ for the four projections.
- The /daily_deltas/ subdirectory contains daily CMIP6-based 'delta' files of T_{min}, T_{max}, precipitation, and relative humidity.
- The /extremes/ subdirectory contains counts of frequency of surpassing extreme thresholds for each of the variables.

Table 1. CHC-CMIP6 data types

Category	Variables	Domain	Columns x Rows	Scenarios
Core	CHIRPS (precipitation)	50°S-50°N	7200x2000	Observational, 2030_SSP245, 2030_SSP585, 2050_SSP245, 2050_SSP585
	$CHIRTS_{max}$ (T_{max})	60°S-60°N	7200x2600	
	$CHIRTS_{min}$ (T_{min})	60°S-60°N	7200x2600	
	RH_n	60°S-60°N	7200x2600	
	RH_x	60°S-60°N	7200x2600	
	RH_{ave}	60°S-60°N	7200x2600	
	HI_{max}	60°S-60°N	7200x2600	
	$WBGT_{max}$	60°S-60°N	7200x2600	
	VPD	60°S-60°N	7200x2600	
	SVP	60°S-60°N	7200x2600	
	precipitation	90°S-90°N	3600x1800	

Deltas	RH_{ave}	90°S-90°N	3600x1800	2030_SSP245, 2030_SSP585, 2050_SSP245, 2050_SSP585
	T_{max}	90°S-90°N	3600x1800	
	T_{min}	90°S-90°N	3600x1800	
Extremes	CHIRPS (precipitation)	50°S-50°N	7200x2000	Observational, 2030_SSP245, 2030_SSP585, 2050_SSP245, 2050_SSP585
	$CHIRTS_{max}$ (T_{max})	60°S-60°N	7200x2600	
	$CHIRTS_{min}$ (T_{min})	60°S-60°N	7200x2600	
	$WBGT_{max}$	60°S-60°N	7200x2600	
	VPD	60°S-60°N	7200x2600	

Note, the overall dataset is large: uncompressed, the dataset is ~ 16 Terabytes total. We advise working with subsets of the data.

2. Methods

The process for creating the CHC-CMIP6 data products is outlined here and further detailed in Figure 1 and the following subsections. The CHC-CMIP6 dataset builds on high-resolution temperature and precipitation products developed by the Climate Hazard Center; relative humidity data from ERA5; and large ensembles of coarse resolution CMIP6 simulations of temperature, precipitation, and relative humidity (Section 2.A). These data were used to create high-resolution projections (Fig. 1). The CMIP6 simulations (Fig. 1A) were used to calculate 2030 and 2050 'deltas'—or mean changes between the current and projection periods—for temperature, humidity, and precipitation (Fig. 1B, Section 2.B). Next, these 'delta' files were combined with the high-resolution observations (Fig. 1C) to produce high-resolution 2030 and 2050 projections of temperature, precipitation, and relative humidity for the two CMIP6 scenarios (SSP245 and SSP585) (Fig. 1D, Section 2.C). Finally, $WBGT_{max}$ (Section 2.D) and VPD (Section 2.E) were derived for the observational (1983-2016) period using the observed temperature and RH fields, and for the projections using the projected temperature and RH fields. Finally, extremes data layers were calculated for the observational period and the four projections (Section 2.F).

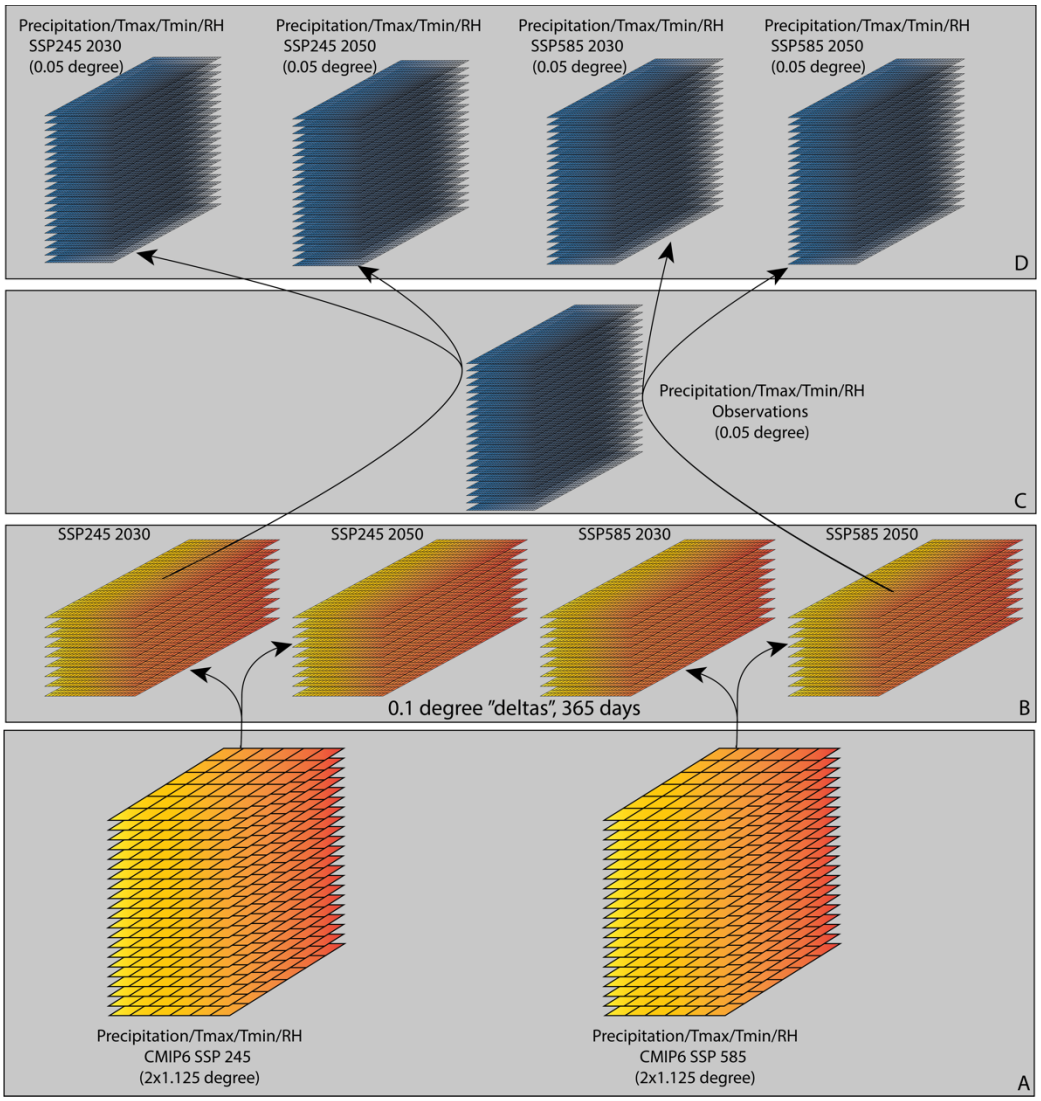

Figure 1. Process schema for the development of the CHC-CMIP6 0.05º datasets. Large ensembles of CMIP6 precipitation, T_{max}, T_{min} and RH simulations (A) were used to calculate monthly "delta" (change) estimates for 2030 and 2050, which are reprojected in space and time to produce global 0.1º daily delta files (B). The daily deltas were then combined with observed precipitation, T_{max}, T_{min} and RH (C) to produce high resolution time-varying data sets incorporating the CMIP6 changes between 1983-2016 and 2025-2035 and 2045-2055 (D).

2.A. Data

The CHC Precipitation (CHIRPS) and Temperature (CHIRTS) Products

The CHC-CMIP6 dataset is partially based on the Climate Hazards Center (CHC) precipitation and temperature products: Climate Hazards InfraRed Precipitation with Stations (CHIRPS) (Funk et al. 2015b) and the Climate Hazards InfraRed Temperature with Stations

(CHIRTS-daily) (Funk et al. 2019; Verdin et al. 2020). The CHC has developed a three-step process that leverages the power of satellite observations to create the high-resolution CHIRPS and CHIRTS products. The use of satellite observations allows for creating high resolution data which captures valuable information about local changes in meteorological variables, especially in data sparse regions of the global south, which is where many of the impacts of climate change are likely to be, and have been, felt most keenly.

The first step in this process involves the development of high resolution (0.05°) precipitation and temperature climatologies (Funk et al. 2015a). The Climate Hazards Center precipitation climatology (CHP_{clim}) was derived from combining satellite-based rainfall estimates with station data and elevation. These long-term mean fields benefit from satellite-based observations, and are particularly suited to data-sparse regions. For example, in Ethiopia, where mean precipitation changes dramatically over short spatial distances, the local variations in climate conditions are captured by CHP_{clim} (Figure 2, reproduced from Funk et al. 2015a). The CHIRTS climatology product (CHT_{clim}) is similarly based on cloud-screened satellite observations of thermal infrared brightness temperatures, which also provides detailed information, even in areas with sparse observation networks (Funk et al. 2019; Verdin et al. 2020).

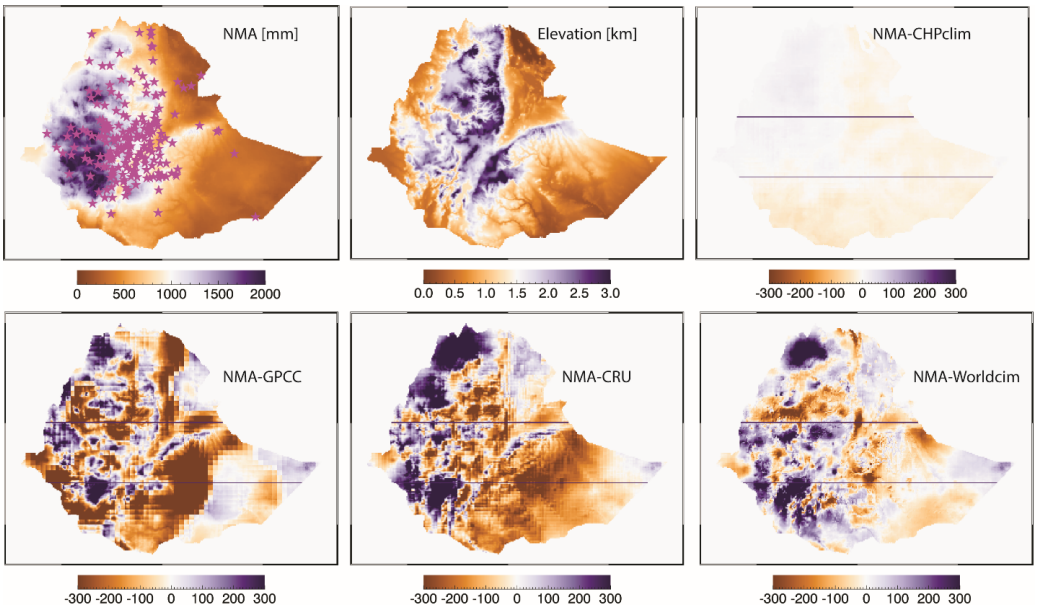

Figure 2. Figure 11 from 'A global satellite assisted precipitation climatology' (Funk et al. 2015a). The upper-left panel shows a 'best estimate' of annual rainfall totals derived using a dense of station normals provided by the Ethiopian National Meteorological Agency (NMA). The upper-right panel shows the differences between the NMA totals and CHP_{clim}. The bottom panels display similar difference plots based on comparisons with the Global Precipitation Climatology Center (GPCC) (Becker et al. 2013; Schneider et al. 2014), Climatic Research Unit (CRU) (New et al. 2002; New et al. 1999), and Worldclim climatologies (Hijmans et al. 2005).

The next step involves combining gridded 0.05° geostationary thermal infrared data (TIR) with the 0.05° climatologies to produce satellite-only CHIRT and CHIRP. Ultimately, CHIRP relies on the satellites' ability to see cold cloud tops, while CHIRT relies on direct observations of the non-cloudy land surface. Both types of observations take advantage of the fact that cloud tops tend to be much colder than surface temperatures.

The final step involves the addition of station observations, resulting in the CHIRPS and CHIRTS. The development process underlying these products, however, is different. It is relatively easy to obtain reliable and rapidly updated satellite-observations of cloud top temperatures, supporting rapid updates of the CHIRPS. Obtaining reliable estimates of surface temperatures is more difficult and requires inter-satellite calibration. Hence, the CHIRTS product currently ends in 2016.

Relative Humidity

The CHC-CMIP6 dataset also includes RH derived from the hourly air temperature (Ta) and dewpoint temperature (Td) from the ERA5 reanalysis (Hersbach et al. 2020) alongside CHIRTS daily T_{max} and T_{min}. RH was calculated using a dewpoint temperature approach, by calculating saturation vapor pressure (SVP)—or the water holding *capacity* of the air at a certain temperature—and actual vapor pressure (AVP)—a function of the actual water content of the air, which are each a function of air temperature and dewpoint temperature, respectively (Daly et al. 2015; Ficklin and Novick 2017).

SVP is an exponential function of air temperature:

$$SVP = 0.611 * exp\left(\frac{17.3 * T_a}{T_a + 273.3}\right)$$

Similarly, AVP is calculated as a function of dewpoint temperature:

$$AVP = 0.611 * exp\left(\frac{17.3 * T_d}{T_d + 273.3}\right)$$

RH is the ratio between AVP and SVP:

$$RH = \frac{AVP}{SVP} * 100$$

Two values of RH were calculated. Generally, in a day, RH peaks when temperatures are at their minimum. RH was derived for the hour of T_{max} of the day (RH_x) for use in calculating daily $WBGT_{max}$. RH_x thus was calculated using CHIRTS daily T_{max} and ERA5 Td at the hour of T_{max}. Additionally, to derive VPD, the daily average RH (RH_{ave}) was derived--SVP was calculated as the mean of SVP_{min} and SVP_{max} (created using CHIRTS daily T_{min} and T_{min}, respectively), with daily averaged ERA5 Td. These daily reanalysis-based humidity fields were regridded to 0.05 degrees.

CMIP6

Projections of changes in meteorological variables were accessed from the Coupled Model Intercomparison Project phase 6 (CMIP6). Accounting for the fact that the extent of future increases in radiative forcing is dependent on both the current and future rate of emissions, and is therefore not fixed, we use two scenarios from CMIP6—Shared Socioeconomic Pathway (SSP) 2-4.5 and SSP 5-8.5 (Meinshausen et al. 2020). The SSP 2-4.5 scenario is based on projections of large increases in sustainable development (SSP2) and 4.5 W m^{-2} of radiative forcing, while SSP 5-8.5 is a scenario of projected further fossil fuel development and increased global market integration (SSP5) with 8.5 W m^{-2} of radiative forcing by 2100. These are generally considered the most likely scenario (SSP245) and the worst-case scenario (SSP585) (Fricko et al. 2017).

CMIP6 data were accessed from Lawrence Livermore National Laboratory (LLNL) node of the Earth System Grid Federation (ESGF) platform (https://esgf-node.llnl.gov/search/cmip6/). Monthly average near-surface relative humidity (hurs), near-surface minimum and maximum temperature (tasmin, tasmax), precipitation (pr), and sea-surface temperature (tos) were retrieved for 26 models for three experiments—historical (1850-2014), and SSP245 and SSP585 (2015-2100). Within each model, the same ensemble members were selected for the historical and future scenario experiments. In total, 152 simulations across 25 models were retrieved for the historical and SSP245 experiments, while 167 were retrieved across the same 25 models for the historical and SSP585 (Table 2).

Next, spatio-temporal cubes (1850-2050) for each variable (hurs, tasmax, tasmin, pr) and experiment (SSP245 and SSP585) were created (Figure 1A). Historical and projection data were stacked using the netCDF Record Concatenator utility (ncrcat). The cubes were then resampled to 100km resolution using bilinear interpolation with the Climate Data Operator (CDO) software *remapbil* utility. For each variable and scenario, the mean was taken for each model across all simulations to derive the model mean, and then the multi-model mean was taken to derive the ensemble mean.

As such, four scenarios were created—2030_SSP245, 2030_SSP585, 2050_SSP245, and 2050_SSP585.

Table 2. CMIP6 models and simulations used.

Model	Spatial Resolution	SSP245 : # sims	SSP585: # sims	Model	Spatial Resolution	SSP245: # sims	SSP585: # sims
ACCESS-CM2	250 km	3	3	GFDL-ESM4	100 km	3	1
ACCESS-ESM1-5	250 km	11	10	GISS-E2-1-G	250 km	10	5
CMCC-ESM2	100 km	1	1	HadGEM3-GC31-LL	250 km	1	4

CNRM-CM6-1	250 km	6	6	INM-CM4-8	100 km	1	1
CNRM-CM6-1-HR	50 km	1	1	INM-CM5-0	100 km	1	1
CNRM-ESM2-1	250 km	9	5	IPSL-CM6A-LR	250 km	11	6
CanESM5	500 km	25	25	MIROC-ES2L	500 km	30	10
CanESM5-CanOE	500 km	3	3	MIROC6	250 km	3	50
EC-Earth3-CC	100 km	1	1	MPI-ESM1-2-HR	100 km	2	2
EC-Earth3-Veg	100 km	5	6	MPI-ESM1-2-LR	250 km	9	10
EC-Earth3-Veg-LR	100 km	3	3	MRI-ESM2-0	100 km	1	1
FGOALS-g3	250 km	4	4	UKESM1-0-LL	250 km	5	5
FIO-ESM-2-0	100 km	3	3				

2.B. Delta Fields

Daily 'deltas' for T_{min}, T_{max}, RH_{ave}, and precipitation were calculated for each pixel, representing the change in each variable between the observational record (1983-2016) and the four CMIP6 scenarios (2030_SSP245, 2030_SSP585, 2050_SSP245, 2050_SSP585) (Figure 2B). The 'deltas' were first calculated as monthly differences between the two periods as follows:

The T_{max}, T_{min}, and RH_{ave} deltas we calculated using arithmetic differences:

$$\Delta 2030_{monthly} = Mean(2025\text{-}2035)_{monthly} - Mean(1983\text{-}2016)_{monthly}$$

$$\Delta 2050_{monthly} = Mean(2045\text{-}2055)_{monthly} - Mean(1983\text{-}2016)_{monthly}$$

The precipitation deltas were calculated as ratios*:

$$\Delta 2030_{monthly} = [Mean(2025\text{-}2035)_{monthly} + \varepsilon]/[Mean(1983\text{-}2016)_{monthly} + \varepsilon]$$

$$\Delta 2050_{monthly} = [Mean(2045\text{-}2055)_{monthly} + \varepsilon]/[Mean(1983\text{-}2016)_{monthly} + \varepsilon]$$

**Precipitation is in units of millimeters per month, and ε is set to 7 millimeters, a value found reasonable based on the production of the CHIRPS dataset.*

For each pixel and variable, monthly data were temporally downscaled to daily data. For a 14-month period -- for each calendar year, including the preceding and following month of the year (Dec_{year-1} … Jan_{year+1}) -- the monthly value was first assigned to each of the daily values for that month. This 14-month-long daily time series was iteratively smoothed, and then the first and last month were discarded, resulting in daily data for that year. These daily data were then further adjusted so that the daily data mean (temperature) or sum (precipitation) across each month equals the original monthly value. These daily deltas were rescaled to a global 0.1° resolution.

2.C. Calculating projected T_{min}, T_{max}, RH, and precipitation for the four scenarios

The daily observational T_{min}, T_{max}, precipitation, and RH_x, and RH_{ave} data were then perturbed using the corresponding delta fields to create the relevant data for the four scenarios. Note that the RH_{ave} deltas were used to perturb both the observational RH_x and RH_{ave} fields. These datasets correspond to the same period of record as the original observations, resulting in daily projections for 2030 (2030_SSP245, 2030_SSP585) and 2050 (2050_SSP245, 2050_SSP585).

A single, stationary delta value was used for each day, location, and variable. For example, the same January 1st T_{max} delta was applied to the 1983 January 1st T_{max} as the 2016 January 1st T_{max} value. Furthermore, no attempt was made to detrend the underlying observational datasets. The benefit of the chosen approach is transparency. We can explicitly map and understand the delta fields, and their implications for changes in the distribution of the daily values.

Once the daily T_{min}, T_{max}, and RH_x, and RH_{ave} data were projected, daily $WBGT_{max}$ (Section 2.D) and VPD (Section 2.E) fields were calculated as well.

2.D. Calculating observed & projected $WBGT_{max}$

In this data set, as in (Tuholske et al. 2021), we calculated maximum $WBGT_{max}$, because we are interested in peak heat stress values that typically occur in the afternoon when air temperatures and relative humidity typically reach their warmest and lowest values, respectively. $WBGT_{max}$ therefore is based on T_{max} and RH_x.

Following (Tuholske et al. 2021), we first calculated Heat Index (HI_{max}) values according to National Ocean and Atmospheric Administration's (NOAA) guidelines (NOAA 2021). Equations for HI_{max} may be found in the NOAA (2021) reference and in the accompanying code for this research. These HI_{max} values were used to estimate $WBGT_{max}$ (Bernard and Iheanacho 2015). The full WBGT estimation process includes radiant heat and wind speeds, but indoor or shaded WBGT (°C) with fixed air speeds (0.5 m/s) can be estimated closely by a quadratic transform of daily HI_{max} (°F) values following Bernard and Iheanacho 2015:

$$WBGT_{max}(°C) = -0.0034HI_{max}{}^2\ (°F) + 0.96HI_{max}(°F) - 34$$

The observed (1983-2016) $WBGT_{max}$ fields were calculated using the above equation and the observed T_{min}, T_{max}, and RH_x fields, while the projected $WBGT_{max}$ fields were derived from the four scenarios of T_{min}, T_{max}, and RH_x.

2.E. Calculating VPD

VPD was calculated based on T_{min}, T_{max}, and RH_{ave}. VPD is simply the arithmetic difference between SVP and AVP:

$$VPD = SVP - AVP$$

The observed (1983-2016) VPD fields were calculated using the observed T_{min}, T_{max}, and RH_{ave} fields, while the projected VPD fields were derived from the four scenario-projections of T_{min}, T_{max}, and RH_{ave}.

2.F Defining & Calculating Extremes:

To support the analysis of shifts in climate extremes in the current climate and simulated future climates, the CHC-CMIP6 product also includes data layers for extremes for T_{min}, T_{max}, precipitation, $WBGT_{max}$, and VPD for the five scenarios (observations, 2030_SSP245, 2030_SSP585, 2050_SSP245, and 2050_SSP585).

For the temperature-related data, extremes are available by month, depicting the number of days for each month experiencing an 'extreme' (T_{min}, T_{max}, $WBGT_{max}$, and VPD). For precipitation, data layers are coded as binaries of whether the monthly total precipitation was classified as an extreme (1) or not (0). For the temperature related fields (T_{min}, T_{max}, VPD, and $WBGT_{max}$), extreme counts are based on daily data, processed on a monthly basis. Validations of daily T_{min} and T_{max} have documented strong performance (Verdin et al. 2019), and in this data descriptor we have shown similar strong performance for VPD and $WBGT_{max}$. Precipitation extreme counts are calculated on a monthly basis for two reasons: (1) defined extreme thresholds exist on a monthly, not daily, timescale (see below), and (2) confidence in the CHIRPS product is much higher at the monthly scale than the daily scale, where daily CHIRPS has been shown to underestimate precipitation extremes.

Definitions of extremes for each variable were based on two methods: based on known thresholds and by calculating pixel-specific breakpoints using the 95th and 99th percentile.

Threshold-Based Extremes:

For the temperature-related variables (T_{min}, T_{max}, VPD, and $WBGT_{max}$), for each variable, year, and scenario, the number of days surpassing the corresponding thresholds were calculated, while for precipitation, the number of months below the fixed threshold were calculated. These fixed thresholds were identified from previous studies or defined for precipitation, temperature, VPD, and $WBGT_{max}$, above which increased impacts occur.

Two thresholds were used for temperatures: 30°C and 40.6°C, representing moderate and extreme heat exposure. These thresholds were chosen based on documented thresholds for agricultural and human heat stress. 30°C has been used to identify agricultural heat stress (Verdin et al. 2020) as inhibition of photosynthetic activity generally begins at or above 30°C (Salvucci and Crafts-Brandner 2004). In health research, heat stroke is defined by when human core body temperature reaches or exceeds 40.6C (Luber and McGeehin 2008). This threshold has been used in studies identifying extreme heat events due to its relationship to human physiology (Mera et al. 2018; Verdin et al. 2020). For precipitation, the threshold of 100 mm per month was utilized. This

threshold was selected based on typical monthly crop water requirements used in crop models (Verdin and Klaver 2002). Two thresholds were used for $WBGT_{max}$: 28°C and 30°C (Tuholske et al. 2021). A $WBGT_{max}$ value of 28°C is defined by the International Standards Organization as the threshold for risk of heat-related illness for acclimated persons at moderate metabolic rates, while 30°C is the threshold for group of persons at low metabolic rates (Tuholske et al. 2021). Finally, we defined two thresholds for VPD: 2kPa and 3kPa. Studies have found that stomatal closure begins when VPD increases above 2 kPa (Lobell et al. 2014; Sadok and Sinclair 2009; Zhang et al. 2019), and GPP exhibits a decline for sites and times when VPD exceeds 2kPa (Zhang et al. 2019). When VPD surpasses 3kPa, evaporative demand can be too high for certain plant types to offset via mitigation strategies (Massmann et al. 2018). Furthermore, few sites experience VPD greater than 3kPa.

Percentile-Based Extremes:

Percentiles were defined for each pixel based on the observed data. For T_{min}, T_{max}, VPD, and $WBGT_{max}$, for each pixel, the daily 95th and 99th percentiles were calculated using 1983-2016 daily data, resulting in a 95th and 99th percentile value for each variable. For each of these four variables, each year (1983-2016), and each of the five scenarios, pixel-wise, the number of days for each month were calculated that surpass these percentile-defined extreme values. For precipitation, both low and high percentile-based extremes were calculated: the corresponding values for monthly precipitation falling lower than the 20th percentile and higher than the 95th percentile were calculated, and these values used for each year across the five scenarios.

The extremes data layers are:

	Naming Convention	Data Layer
1	Daily_VAR_MM_95th_pctile.tif *(observations scenario only)*	The breakpoint value (in units of variable) for the 95th percentile for all days in month from 1983-2016
2	Daily_VAR_MM_95th_pctile.tif *(observations scenario only)*	The breakpoint value (in units of variable) for the 99th percentile for all days in month from 1983-2016
3	Daily_VAR_YYYY_MM_cnt_VARgtTHRESH1.tif	Count of # days above the 1st defined fixed threshold
4	Daily_VAR_YYYY_MM_cnt_VARgtTHRESH2.tif	Count of # days above the 2nd defined fixed threshold
5	Daily_VAR_YYYY_MM_cnt_VARgt95.tif	Count of # days above the breakpoint (#1) for the 95th percentile
6	Daily_VAR_YYYY_MM_cnt_VARgt99.tif	Count of # days above the breakpoint (#2) for the 99th percentile
7	Daily_VAR_YYYY_MM_monthly_mean.tif	Mean monthly value for the variable

References:

Ahrens, C. D. (1994). Meteorology today. An introduction to weather, Climate, and the environment.

Becker, A., Finger, P., Meyer-Christoffer, A., Rudolf, B., Schamm, K., Schneider, U., and Ziese, M. (2013). A description of the global land-surface precipitation data products of the Global Precipitation Climatology Centre with sample applications including centennial (trend) analysis from 1901–present, Earth Syst. Sci. Data, 5, 71–99, doi:10.5194/essd-5-71-2013.

Bernard, T. E., and I. Iheanacho, 2015: Heat index and adjusted temperature as surrogates for wet bulb globe temperature to screen for occupational heat stress. Journal of Occupational and Environmental Hygiene, 12, 323-333.

Budd, Grahame M. "Wet-bulb globe temperature (WBGT)—its history and its limitations." Journal of science and medicine in sport 11, no. 1 (2008): 20-32.

Bynum, G. D., and Coauthors, 1978: Induced hyperthermia in sedated humans and the concept of critical thermal maximum. American Journal of Physiology-Regulatory, Integrative and Comparative Physiology, 235, R228-R236.

Chapin, S. F., Matson, P. A., & Vitousek, P. M. (2012). Water and Energy Balance. In Principles of Terrestrial Ecosystem Ecology (pp. 1-529). https://doi.org/10.1007/978-1-4419-9504-9

Cheung, S. S., and T. M. McLellan, 1998: Heat acclimation, aerobic fitness, and hydration effects on tolerance during uncompensable heat stress. Journal of applied physiology.

Daly, C., Smith, J. I., & Olson, K. v. (2015). Mapping atmospheric moisture climatologies across the conterminous United States. In PLoS ONE (Vol. 10, Issue 10). https://doi.org/10.1371/journal.pone.0141140

Ficklin, D. L., & Novick, K. A. (2017). Historic and projected changes in vapor pressure deficit suggest a continental-scale drying of the United States atmosphere. Journal of Geophysical Research, 122(4), 2061-2079. https://doi.org/10.1002/2016JD025855

Fricko, O., Havlik, P., Rogelj, J., Klimont, Z., Gusti, M., Johnson, N., ... & Riahi, K. (2017). The marker quantification of the Shared Socioeconomic Pathway 2: A middle-of-the-road scenario for the 21st century. Global Environmental Change, 42, 251-267.

Fu, Z., Ciais, P., Prentice, I. C., Gentine, P., Makowski, D., Bastos, A., Luo, X., Green, J. K., Stoy, P. C., Yang, H., & Hajima, T. (2022). Atmospheric dryness reduces photosynthesis along a large range of soil water deficits. Nature Communications, 13(1). https://doi.org/10.1038/s41467-022-28652-7

Funk, C., A. Verdin, J. Michaelsen, P. Peterson, D. Pedreros, and G. Husak, 2015a: A global satellite assisted precipitation climatology. Earth Syst. Sci. Data Discuss., 7, 1-13.

Funk, C., and Coauthors, 2015b: The climate hazards infrared precipitation with stations—a new environmental record for monitoring extremes. Scientific data, 2.

Funk, C., and Coauthors, 2019: A High-Resolution 1983–2016 Tmax Climate Data Record Based on Infrared Temperatures and Stations by the Climate Hazard Center. Journal of Climate, 32, 5639-5658.

Grossiord, C., Buckley, T. N., Cernusak, L. A., Novick, K. A., Poulter, B., Siegwolf, R. T. W., Sperry, J. S., & McDowell, N. G. (2020). Plant responses to rising vapor pressure deficit. *New Phytologist*, *226*(6), 1550–1566. https://doi.org/10.1111/nph.16485

He, B., Chen, C., Lin, S., Yuan, W., Chen, H. W., Chen, D., Zhang, Y., Guo, L., Zhao, X., Liu, X., Piao, S., Zhong, Z., Wang, R., & Tang, R. (2022). Worldwide impacts of atmospheric vapor pressure deficit on the interannual variability of terrestrial carbon sinks. National Science Review. https://doi.org/10.1093/nsr/nwab150

Held, I. M., & Soden, B. J. (2006). Robust responses of the hydrological cycle to global warming. Journal of climate, 19(21), 5686-5699.

Hersbach, H., and Coauthors, 2020: The ERA5 global reanalysis. Quarterly Journal of the Royal Meteorological Society, 146, 1999-2049.

Hijmans, R. J., Cameron, S. E., Parra, J. L., Jones, P. G., and Jarvis, A. (2005). Very high resolution interpolated climate surfaces for global land areas, Int. J. Climatol., 25, 1965–1978.

ISO, c., 2017: Ergonomics of the Thermal Environment—Assessment of Heat Stress Using the WBGT (Wet Bulb Globe Temperature) Index (ISO 7243: 2017). International Organization for Standardization Geneva, Switzerland.

Kath, J., Craparo, A., Fong, Y., Byrareddy, V., Davis, A. P., King, R., ... & Power, S. (2022). Vapour pressure deficit determines critical thresholds for global coffee production under climate change. Nature Food, 1-10.

Kong, Q., & Huber, M. (2022). Explicit Calculations of Wet-Bulb Globe Temperature Compared With Approximations and Why It Matters for Labor Productivity. Earth's Future, 10(3), e2021EF002334.

Lobell, D. B., Roberts, M. J., Schlenker, W., Braun, N., Little, B. B., Rejesus, R. M., & Hammer, G. L. (2014). Greater sensitivity to drought accompanies maize yield increase in the U.S. Midwest. Science, 344(6183), 516-519. https://doi.org/10.1126/science.1251423

Luber, G., & McGeehin, M. (2008). Climate change and extreme heat events. American journal of preventive medicine, 35(5), 429-435.

Massmann, A., Gentine, P., & Lin, C. (2018). When does vapor pressure deficit drive or reduce evapotranspiration? Journal of Advances in Modeling Earth Systems. https://doi.org/10.5194/hess-2018-553

Meinshausen, M., Nicholls, Z. R. J., Lewis, J., Gidden, M. J., Vogel, E., Freund, M., Beyerle, U., Gessner, C., Nauels, A., Bauer, N., Canadell, J. G., Daniel, J. S., John, A., Krummel, P. B., Luderer, G., Meinshausen, N., Montzka, S. A., Rayner, P. J., Reimann, S., Smith, S. J., van den Berg, M., Velders, G. J. M., Vollmer, M. K., and Wang, R. H. J. (2020). The shared socio-economic pathway (SSP) greenhouse gas concentrations and their extensions to 2500, Geosci. Model Dev., 13, 3571–3605, https://doi.org/10.5194/gmd-13-3571-2020, 2020.

Mera, R., Massey, N., Rupp, D. E., Mote, P., Allen, M., & Frumhoff, P. C. (2015). Climate change, climate justice and the application of probabilistic event attribution to summer heat extremes in the California Central Valley. Climatic Change, 133(3), 427-438.

Mora, C., and Coauthors, 2017: Global risk of deadly heat. Nature climate change, 7, 501-506.

New, M., Hulme, M., and Jones, P. (1999). Representing twentieth-century space–time climate variability. Part I: Development of a 1961–90 mean monthly terrestrial climatology, J. Climate, 12, 829–856.

New, M., Lister, D., Hulme, M., and Makin, I. (2002). A high-resolution data set of surface climate over global land areas, Climate Res., 21, 1–15, doi:10.3354/cr021001.

NOAA: The heat index equation. [Available online at https://www.wpc.ncep.noaa.gov/html/heatindex_equation.shtml.]

Novick, K. A., Ficklin, D. L., Stoy, P. C., Williams, C. A., Bohrer, G., Oishi, A. C., Papuga, S. A., Blanken, P. D., Noormets, A., Sulman, B. N., Scott, R. L., Wang, L., & Phillips, R. P. (2016). The increasing importance of atmospheric demand for ecosystem water and carbon fluxes. *Nature Climate Change*, *6*(11), 1023–1027. https://doi.org/10.1038/nclimate3114

Pradhan, B., T. Kjellstrom, D. Atar, P. Sharma, B. Kayastha, G. Bhandari, and P. K. Pradhan, 2019: Heat stress impacts on cardiac mortality in Nepali migrant workers in Qatar. Cardiology, 143, 37-48.

Rao, K., Williams, A. P., Diffenbaugh, N. S., Yebra, M., Konings, A. G. (2022). Plant-water sensitivity regulates wildfire vulnerability. Nature Ecology and Evolution. https://doi.org/10.1038/s41559-021-01654-2

Sadok, W., & Sinclair, T. R. (2009). Genetic variability of transpiration response to vapor pressure deficit among soybean cultivars. Crop Science, 49(3), 955-960.

Salvucci, M. E., & Crafts-Brandner, S. J. (2004). Inhibition of photosynthesis by heat stress: the activation state of Rubisco as a limiting factor in photosynthesis. Physiologia plantarum, 120(2), 179-186.

Schneider, U., Becker, A., Finger, P., Meyer-Christoffer, A., Ziese, M., and Rudolf, B. (2014). GPCC's new land surface precipitation climatology based on quality-controlled in situ data and its role in quantifying the global water cycle. Theor. and Appl. Clim., 115, 15–40.

Sperry, J. S., Venturas, M. D., Anderegg, W. R. L., Mencuccini, M., Mackay, D. S., Wang, Y., & Love, D. M. (2017). Predicting stomatal responses to the environment from the optimization of photosynthetic gain and hydraulic cost. Plant Cell and Environment, 40(6), 816-830. https://doi.org/10.1111/pce.12852

Tague, C. (2022). The bedrock of forest drought. Nature Geoscience, 1-2.

Tuholske, C., Caylor, K., Funk, C., Verdin, A., Sweeney, S., Grace, K., ... & Evans, T. (2021). Global urban population exposure to extreme heat. *Proceedings of the National Academy of Sciences*, *118*(41), e2024792118.

Verdin, A., C. Funk, P. Peterson, M. Landsfeld, C. Tuholske, and K. Grace, 2020: Development and validation of the CHIRTS-daily quasi-global high-resolution daily temperature data set. Scientific Data, 7, 1-14.

Verdin, J., & Klaver, R. (2002). Grid-cell-based crop water accounting for the famine early warning system. Hydrological Processes, 16(8), 1617-1630.

Williams, A. P., Cook, E. R., Smerdon, J. E., Cook, B. I., Abatzoglou, J. T., Bolles, K., ... & Livneh, B. (2020). Large contribution from anthropogenic warming to an emerging North American megadrought. *Science*, *368*(6488), 314-318.

Zhang, Q., Ficklin, D. L., Manzoni, S., Wang, L., Way, D., Phillips, R. P., & Novick, K. A. (2019). Response of ecosystem intrinsic water use efficiency and gross primary productivity to rising vapor pressure deficit. Environmental Research Letters, 14(7). https://doi.org/10.1088/1748-9326/ab2603